

# Measuring Shallow Convective Mass Flux Profiles in the Trade Wind Region

MARCUS KLINGEBIEL,<sup>a</sup> HEIKE KONOW,<sup>b</sup> AND BJORN STEVENS<sup>a</sup>

<sup>a</sup> *Max-Planck-Institut für Meteorologie, Hamburg, Germany*

<sup>b</sup> *Universität Hamburg, Hamburg, Germany*

(Manuscript received 17 November 2020, in final form 7 June 2021)

**ABSTRACT:** Mass flux is a key quantity in parameterizations of shallow convection. To estimate the shallow convective mass flux as accurately as possible, and to test these parameterizations, observations of this parameter are necessary. In this study, we show how much the mass flux varies and how this can be used to test factors that may be responsible for its variation. Therefore, we analyze long-term Doppler radar and Doppler lidar measurements at the Barbados Cloud Observatory over a time period of 30 months, which results in a mean mass flux profile with a peak value of  $0.03 \text{ kg m}^{-2} \text{ s}^{-1}$  at an altitude of  $\sim 730 \text{ m}$ , similar to observations from Ghate et al. at the Azores Islands. By combining Doppler radar and Doppler lidar measurements, we find that the cloud-base mass flux depends mainly on the cloud fraction and refutes an idea based on large-eddy simulations that the velocity scale is in major control of the shallow cumulus mass flux. This indicates that the large-scale conditions might play a more important role than what one would deduce from simulations using prescribed large-scale forcings.

**KEYWORDS:** Tropics; Cumulus clouds; Mass fluxes/transport; Lidars/Lidar observations; Radars/Radar observations

## 1. Introduction

Shallow cumulus clouds play an important role for the global climate system, are very common in the trade wind regions (Nuijens et al. 2014), and are therefore the subject of many studies (e.g., Stevens 2005; Nuijens et al. 2009; Lamer et al. 2015; Lonitz et al. 2015; Lareau et al. 2018; Bony et al. 2017) going back to the past century (i.e., Riehl 1954). These clouds have sizes smaller than the typical grid size of a Global Circulation Model (GCM) and therefore need to be parameterized in global models (Tiedtke 1989; Albrecht 1981; Bretherton et al. 2004; Neggers et al. 2009). Many shallow cumulus parameterizations are based on a mass flux approach, that predicts the vertical structure of cumulus up- and downdrafts and goes back to the conceptual framework developed by Arakawa and Schubert (1974), who originally defined the mass flux of the  $i$ th cloud, as

$$M_i = \rho w_i a_i, \quad (1)$$

with the air density  $\rho$ , the fraction of area covered by updrafts  $a$ , and the vertical velocity averaged above all updrafts  $w$ . The unit of  $M_i$  is  $\text{kg m}^{-2} \text{ s}^{-1}$ . Parameterizations to represent the collective effects of shallow convection on the larger scales of motion thus set out to model  $M_i$  (or its sum over all cloud types). Testing their capability to do so therefore requires the ability to identify and quantify the mass flux associated with individual clouds. Ghate et al. (2011) used Doppler radar measurements located at an Atmospheric Radiation Measurements (ARM)'s

Mobile Facility station at the Azores islands and showed that mass flux measurements of shallow cumulus are possible. For this purpose, they analyzed 114 h of data sampled over 4 months. In their results they present mass flux and vertical velocity profiles of shallow cumulus, which both maximize near cloud base. A larger dataset with 3009 h of measurements was analyzed by Lamer et al. (2015), who used this technique to test the idea—often used in models—that the mass flux is dominated by updrafts, and that the compensating downward mass occurs in the clear air environment away from the clouds. What the previous measurements have not attempted to test, perhaps given limitations in the data they analyzed, are theories considering the variation of the mass flux.

In this paper we will elaborate the question how much the mass flux varies and how this can be used to test factors that may be responsible for its variation. In large-eddy simulations (LES), where large-scale conditions are prescribed, it is shown that the mass flux varies mostly with the surface flux and the depth of the subcloud layer as described by the convective velocity scale, so that regarding to Grant (2001) the cloud-base mass flux  $m_b$  is proportional to the subcloud-layer convective velocity scale  $w_*$ . To test that relationship with observations, we need to be able to measure  $w_*$  and  $m_b$ . Therefore, we show in sections 3 and 4 the parameters which influence  $m_b$  and how a mean mass flux profile is estimated. We identify  $w_*$  in section 5 using a Doppler lidar to measure the velocity inside the boundary layer, not just in clouds. The direct comparison of  $m_b$  and  $w_*$  is also shown in section 5. Our findings are summarized in section 6. Before we go into the measurements and the analysis, we will introduce the instruments and the used dataset in the following section.

## 2. Instrumentation

The Barbados Cloud Observatory (BCO) is located on the east coast of the island of Barbados ( $13.16^\circ\text{N}$ ,  $59.43^\circ\text{W}$ ), which

Klingebiel's current affiliation: Leipziger Institut für Meteorologie, Universität Leipzig, Leipzig, Germany.

Corresponding author: Marcus Klingebiel, marcus.klingebiel@uni-leipzig.de

sits in the trade wind region of the Atlantic Ocean. Since 2010, the BCO has hosted a couple of common meteorological and advanced active and passive remote sensing instruments to explore shallow clouds, circulation and climate sensitivity in the Trades (Stevens et al. 2016). In the following, the two key instruments and the dataset that are used for this study are described.

#### a. Ka-band Doppler cloud radar

To measure cloud fraction based on the echo fraction and the vertical velocity of cloud droplets, a high-power 35.5 GHz (Ka-band) polarized Doppler cloud radar is used. It is a pulsed system that operates in a zenith staring mode and detects cloud particles at an altitude between 156 and 25 972 m, using a range gating of 31.18 m. The radar sensitivity at an altitude of 5 km is  $-52$  dBZ. By using a Doppler technique with an FFT of 256 samples, the Doppler resolution is  $<0.02$  m s $^{-1}$  between  $-10$  and  $+10$  m s $^{-1}$ . Radar calibration and data processing are done by following the procedures given in Gorsdorf et al. (2015). The radar started operating in April 2015 (replacing the Katrin radar) and beginning in July 2018, the temporal resolution of the measurements was changed from 10 to 2 s.

#### b. Doppler lidar

To identify the vertical air motion in the subcloud layer, we use measurements by a HALO Photonics Streamline Pro Doppler-lidar. It measures vertical velocities up to  $\pm 20$  m s $^{-1}$  at altitudes between 155 and approximately 1000 m with an accuracy of  $<0.2$  m s $^{-1}$  for a signal to noise ratio of  $-17$  dB. The temporal resolution is 1.3 s. To sample the same air masses as they pass over the BCO instruments, the Doppler lidar sits on top of the container which houses the Ka-band radar [see Fig. 1 in Klingebiel et al. (2019)].

#### c. Shallow cumulus dataset

Since June 2016, the Doppler radar and Doppler lidar have been measuring simultaneously and operating in a zenith pointing mode at the BCO. To avoid radar echoes from hygroscopically grown sea salt particles, radar reflectivity values less than  $-50$  dBZ are removed. To identify and analyze only shallow cumulus clouds, we use the Konow cloud segmentation algorithm (Konow 2020), which transforms radar observations into connected cloud objects and delivers cloud parameters (e.g., cloud-base/top height, cloud depth, and cloud chord length). This cloud mask was applied before in George et al. (2021) and in Schulz et al. (2021). Based on these parameters, it is easy to exclude clouds other than shallow cumulus by using a simple filter. To neglect precipitating clouds, we filter out all clouds with an echo below 300 m, which is an indicator for precipitation in the applied cloud mask. Midlevel and high-level clouds are filtered out by removing clouds with a cloud base higher than 1 km. The whole dataset that we use in this study consists of 15 201 h covering a time period over 30 months from June 2016 to December 2018.

### 3. Estimation of the mass flux and its influencing factors

As mentioned before, we want to test a hypothesis from Grant (2001), who showed that the mass flux is proportional to

the subcloud-layer velocity scale. For this reason we show in the following how we estimate the mass flux and focus on the influencing parameters.

Based on Eq. (1), we know that the cloud fraction  $a$  and vertical velocity  $w$  influence the shallow convective mass flux. Lamer et al. (2015) showed that the shallow convective mass flux is mainly influenced by the cloud fraction and only secondarily by the vertical velocity. Based on this finding, we will analyze with an enhanced dataset these correlations to show how much cloud fraction and vertical velocity influence the mass flux. In addition we will determine a linear equation, which can be used to calculate the mass flux based on the cloud fraction. That will allow in the future to estimate roughly the mass flux at the BCO by just measuring the cloud fraction. For this reason, we adopt a similar approach that is used by Ghate et al. (2011) and calculate over the entire time period of 30 months (June 2016 to December 2018) the hourly mass flux profiles with

$$M = pwa. \quad (2)$$

Vertical velocity and cloud fraction, both measured by the Ka-band radar over one hour time intervals, are given by  $w$  and  $a$ , respectively. Following Ghate et al. (2011), the air density,  $\rho$ , is assumed to be constant with  $1.2$  kg m $^{-3}$ . For each hourly mass flux profile, the maximum value, which is usually close to cloud base (radar reflectivity  $> -50$  dBZ), is picked and compared with cloud fraction and vertical velocity values at the same height. Only positive mass fluxes were considered to avoid decaying clouds.

The results show a linear relationship of the mass flux with the cloud fraction and the vertical velocity (Fig. 1). As expected from prior studies (Kumar et al. 2015; Lamer et al. 2015), the Pearson correlation coefficient ( $r = 0.8$ ) indicates that the mass flux is mainly influenced by the cloud fraction. The vertical velocity ( $r = 0.47$ ) plays a secondary role. Because there is a strong correlation between cloud fraction and mass flux, we added a linear regression in Fig. 1a, which can be used to roughly estimate the shallow convective mass flux by only knowing the hourly averaged shallow cumulus cloud fraction. Using this regression the convective mass flux for shallow cumulus clouds at the BCO can be estimated with

$$M = \rho wa = 0.45a. \quad (3)$$

With a root-mean-square error of  $0.028$  kg m $^{-2}$  s $^{-1}$  between measurements and predicted values, this method can be used to give a rough idea about the shallow convective mass flux based on the cloud fraction of shallow cumulus clouds.

In summary, we can confirm with the enhanced dataset prior results from Lamer et al. (2015), who showed that the cloud fraction mainly influences the mass flux.

### 4. Mean mass flux profiles and their required sampling times

As previously shown in Lamer et al. (2015) and in section 3, the shallow convective mass flux is mainly influenced by the cloud fraction. But to estimate the cloud-base mass flux and compare it with the velocity scale, like we do it in the next section, we have to know how much the cloud fraction varies

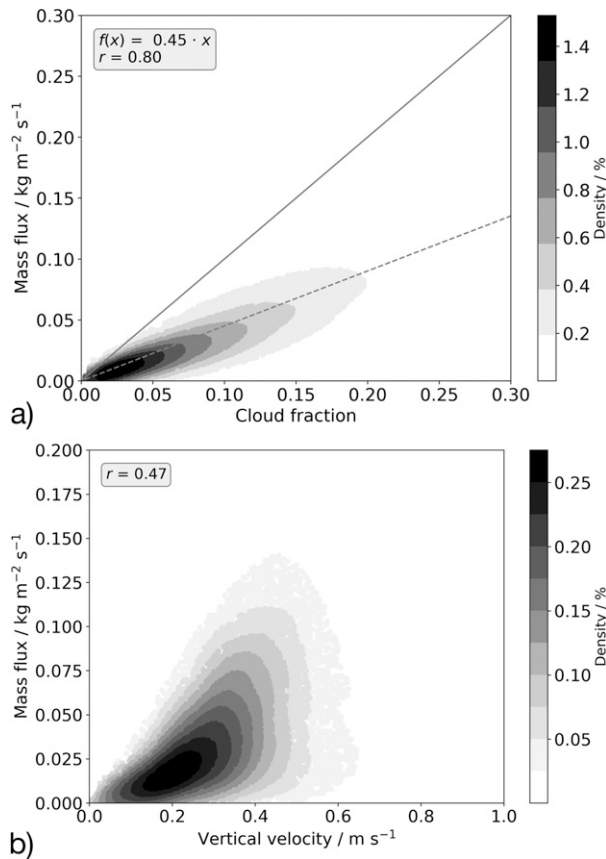


FIG. 1. (a) Correlation between hourly mass flux at cloud base and the associated cloud fraction. The identity line is shown in gray and the dashed line presents the linear regression. (b) Correlation between mass flux and vertical velocity. Both panels consider a dataset taken over 30 months (June 2016–December 2018).

over time and make sure that the sampling interval at the BCO is long enough to get a good estimate of it.

Therefore, we first calculate a mean mass flux profile, based on Eq. (2), by averaging the vertical velocity and the cloud fraction over the 30-month time period (see section 2c). The cloud fraction is calculated by considering only shallow cumulus and clear sky. Other clouds are filtered out by the Konow cloud mask algorithm, including the time span which they cover. Otherwise, the removed clouds would count as clear sky, which would lead to a falsified shallow cumulus cloud fraction. The result is shown in Fig. 2c together with the individual components of the mass flux, the cloud fraction  $a$  (Fig. 2a) and the vertical velocity  $w$  (Fig. 2b). The highest values of the cloud fraction and vertical velocity profile are in an altitude of  $\sim 730$  m, which is  $\sim 170$  m above the averaged cloud-base height. The reason that the maximum values of both parameters appear in a similar altitude is unclear but might be arising from the fact that cloud base and cloud depth vary, which will give a height whereas most clouds are present, as the overlap between those that have formed, and those that formed lower down but have not yet been diminished by mixing. Like shown before, cloud fraction and vertical velocity

influence the mass flux profile (Fig. 2c), which shows a peak value of  $0.03 \text{ kg m}^{-2} \text{ s}^{-1}$ . This result is similar to the measurements from Ghate et al. (2011) (see Fig. 6d in Ghate et al. 2011), even though their measurements considered less shallow cumulus clouds and were observed at different time periods and in another region (the Azores Islands) of the Atlantic Ocean.

The disadvantage of ground based remote sensing measurements unlike satellite measurements or numerical simulations, is that these observations do not cover a larger region. Increasingly it is appreciated how even shallow trade wind clouds organize themselves into mesoscale patterns that can extend for hundreds of kilometers (e.g., Stevens et al. 2020). If we assume the cloud field is stationary one can calculate, for different degrees of organization, how long one needs to sample the flow advecting over a point observation site, to obtain a reasonable estimate of a cloud field of known cloud fraction. We do so by first calculating hourly cloud fraction profiles for all the available data. From the profiles we select the peak value in the altitude range between 460 and 1070 m and calculate its variance. To identify how long we have to measure until the variance is not changing anymore, we average over time periods up to 50 h. The results are given in Fig. 3a (blue line) and show that the time constant, which is calculated by multiplying the initial variance value with  $1/e$ , is reached after an averaging time of 20 h. We take this as indicative of the 20-h-averaged profile being representative of the large-scale cloud fraction.

Nevertheless, the variance of the cloud fraction measurements is influenced on the one hand by the weather conditions, which is expected to cause systematic variations, and on the other hand by the sampling from a fixed point, which leads to random sampling errors. To identify how much the latter is influencing the measurements, we simulate an area of  $560 \text{ km} \times 560 \text{ km}$  with a pixel size of  $100 \text{ m} \times 100 \text{ m}$  and a given cloud cover of 20%. The simulated clouds are given an elliptical shape (see Fig. 3b), because the observed shallow cumulus clouds at Barbados are commonly stretched along the wind direction. Measurements of these clouds are simulated by assuming a horizontal wind speed of  $6.5 \text{ m s}^{-1}$  (it is the mean value of horizontal wind speed measurements from 2011 to 2019 at the BCO) and counting the cloud covered pixels along each pixel row. How many pixels of each row are considered depends on the averaging time. Figure 3c shows that for higher averaging times the spread around the given cloud fraction (0.2) gets less. For each distribution in Fig. 3c, a variance is calculated and shown as orange cross in Fig. 3a. The corresponding time constant of the simulated clouds with a cloud fraction of 20% leads to the conclusion that for sampling intervals longer than 2 h, the sampling uncertainty caused by measurements from a fixed point are negligible. The simulation was also conducted for a cloud fraction of 6% (see Fig. 3a), which represents the measurements in Fig. 2a and leads to a similar result. This approach assumes no large-scale organization in the cloud fields, for instance as might be associated with wind aligned cloud rows, or the forms of mesoscale organization discussed by Stevens et al. (2020), thus, at best it provides a lower bound on the required sampling time.

All in all, the simulated cloud field with a given and well distributed cloud cover shows that the measurements at the BCO are

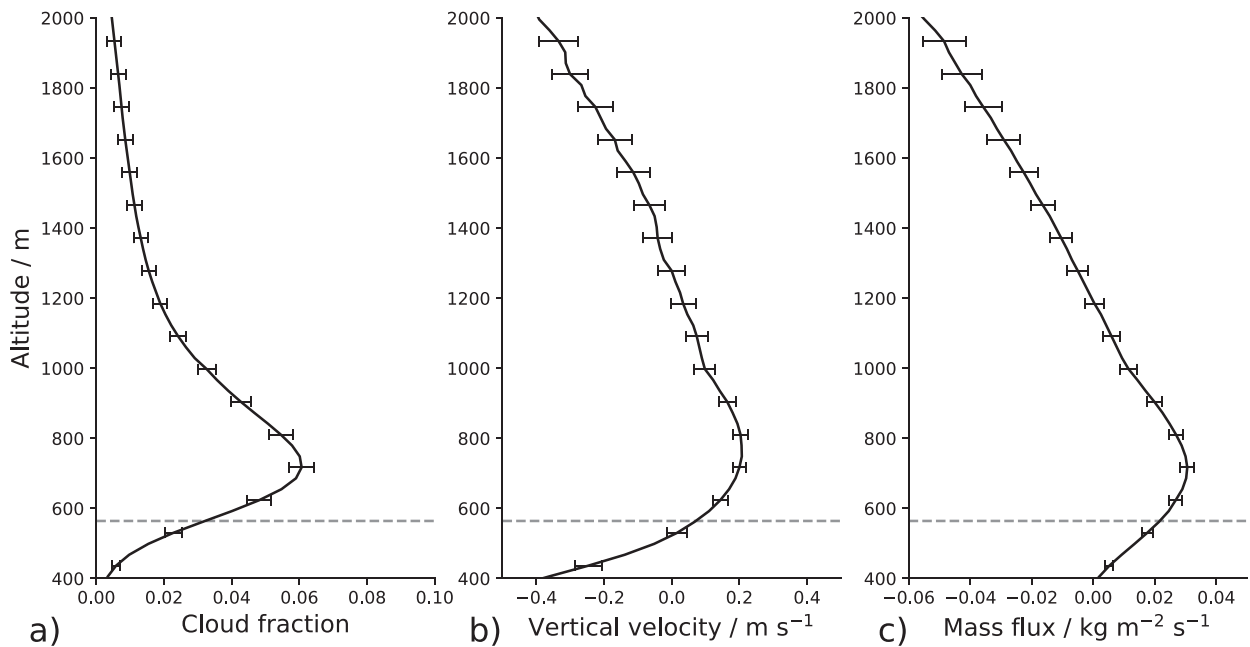


FIG. 2. Typical vertical profiles of (a) cloud fraction and (b) vertical velocity based on Doppler radar measurements from shallow cumulus clouds over a time period of 30 months. (c) Equation (2) is used to calculate the mass flux profile. The horizontal dashed line indicates the averaged cloud-base height and the whiskers show the standard error.

representative when the sampling period is longer than at least 2 h, because after that time the time constant is exceeded. The estimated variance of the observations indicates that the large-scale cloud conditions, which are influenced by the weather conditions, can be covered by sampling periods longer than 20 h. For our further analysis it means that we have to sample at least 2 h to avoid measurement uncertainties because the BCO is a fix point measurement and at least 20 h to get a good estimate of the large-scale cloud fraction. That is why we sample in the following over whole days (24 h), which also removes diurnal variability (Vial et al. 2019).

## 5. Estimating mass flux profiles through the entire boundary layer

In section 4 and in prior studies, mass flux measurements of shallow cumulus clouds were conducted by Doppler radar and wind profiler instruments (Ghate et al. 2011; Lamer et al. 2015; Kumar et al. 2015). This kind of instrumentation was used to estimate cloud fraction and vertical velocity profiles inside clouds. Nevertheless, information about the mass flux below cloud base were not delivered. For this reason, and to test a hypothesis by Grant (2001), who showed with LES that the cloud-base mass flux is just proportional to the subcloud-layer convective velocity scale, we combine in the following Doppler radar and Doppler lidar measurements to get an entire mass flux profile from near the surface to the top of the cloud.

### a. Deriving mass flux profiles from combined cloud and subcloud-layer measurements

Before we can combine Doppler radar and Doppler lidar data, we have to identify if these measurements are

comparable at all, because the vertical velocity measurements of the Doppler lidar and the Ka-band radar are based on different detection methods. Whereas the radar is proportional to the sixth moment of the droplet size spectrum, the lidar is sensitive to the second moment. Hence, for the same amount of mass the lidar return increases with decreasing mean drop size, and the radar return increases with increasing mean drop size. Due to the optical thickness of clouds, the Doppler lidar is only able to measure the vertical motion of cloud particles at the cloud edges. On the other hand, aerosol particles that have not deliquesced, i.e., as found well below the clouds base, are too small to be detected by the radar. It is challenging to compare the vertical velocity measurements of both instruments because they are made for different objectives. However, caused by the high relative humidities and the high horizontal wind speed in the tropical trade wind region, hygroscopically grown sea salt particles are known to be dominant in the sub-cloud layer and can be detected by radar and lidar instruments simultaneously (Klingebiel et al. 2019). Therefore, we are able to compare the radar based vertical velocity measurements of hygroscopically grown sea salt particles ( $D > 5 \mu\text{m}$ ) with the Doppler lidar vertical velocity measurements of aerosol particles. Figure 4 shows vertical velocity measurements from both instruments taken on 14 February 2018. Hygroscopically grown sea salt particles were present over the entire day in the subcloud layer. For this intercomparison, only radar data with a radar reflectivity signal between  $-65$  and  $-50$  dBZ at an altitude up to 750 m were taken into account. These thresholds were chosen to avoid noise and particles other than hygroscopically grown sea salt particles. The temporal and vertical resolution of the Doppler lidar data were interpolated on the

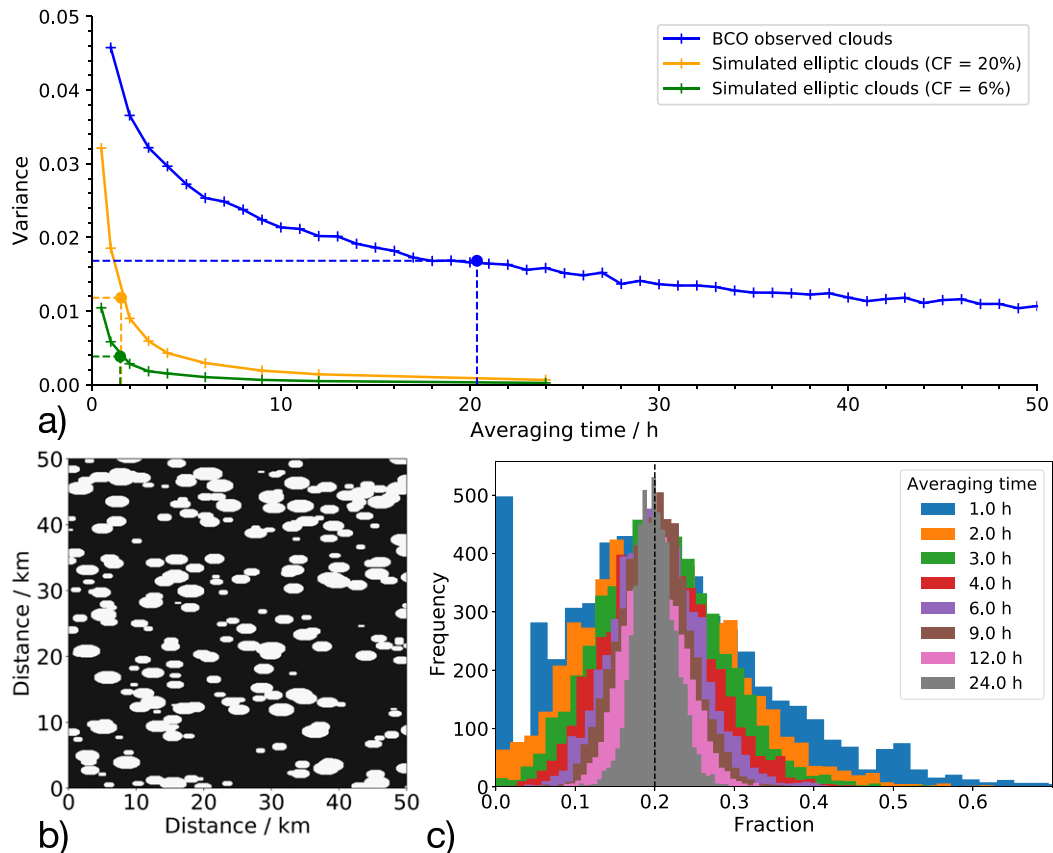


FIG. 3. (a) Variance calculations of cloud fraction for observed and simulated clouds with a cloud fraction of 20% and 6%. The dashed lines indicate the belonging time constants. (b) Subsample of simulated clouds on a 560 km  $\times$  560 km area with a cloud fraction of 20%. (c) Estimated cloud fraction for different sampling periods, based on the cloud simulations from (b). The vertical dashed line indicates the given cloud fraction in the simulations.

resolution from the radar instrument, and the result given in Fig. 4 shows that the vertical velocity measurements of the Ka-band radar are slightly higher (around  $0.1 \text{ m s}^{-1}$ ) than the Doppler lidar. Because this difference is smaller than the given accuracy of the Doppler lidar, we conclude that both instruments can be used for combined vertical velocity measurements.

The similarity of both measurements is also expected on theoretical grounds. Whereas the velocity measured by the lidar is weighted by the motion of the smaller particles, which follow wind and turbulences, the velocity of the radar is weighted by the largest particles and thus more influenced by their fall speed. The bigger the cloud droplets are the bigger is their mass and the related fall velocity. Depending on the droplet diameter, this fall velocity might influence the measurements of the vertical air motion. But even if we assume that the Doppler spectrum is sensitive to the larger cloud droplets, and assume a droplet diameter of  $32.5 \mu\text{m}$  (following Siebert et al. 2013), estimated fall velocities (e.g., Pruppacher and Klett 2010) are about  $0.03 \text{ m s}^{-1}$  and thus substantially smaller than the difference between the lidar and radar Doppler velocities, and on the order of the Doppler resolution of the Ka-band cloud radar to begin with.

The Doppler velocity data from the Ka-band radar and Doppler lidar are combined in a single dataset with the same temporal resolution taking values from the radar inside the clouds and from the lidar below cloud base. For each time step, the cloud base is estimated at the altitude level where the radar reflectivity exceeds a threshold of  $-50 \text{ dBZ}$  to avoid hygroscopically grown sea salt particles. Using this combined dataset, cloud fraction and vertical velocity profiles from 155 m to cloud top can be estimated. To calculate from these parameters the upward  $M_u$  and downward directed mass flux  $M_d$ , we change Eq. (2) to

$$M = \rho a_u w_u + \rho a_d w_d = M_u + M_d. \quad (4)$$

The variables  $a_d$  and  $a_u$  describe the fraction of down- and updrafts, respectively. The velocities of these up- and down-drafts are indicated by  $w_u$  and  $w_d$ .

As an example, we calculate cloud fraction, vertical velocity and mass flux profile for the 28 March 2018. This day was dominated by shallow cumulus, warm rain and midlevel clouds, which is shown by the radar reflectivity in Fig. 5a. The cloud-mask algorithm (see section 2c) is applied to this dataset and identifies each single cloud and delivers the corresponding

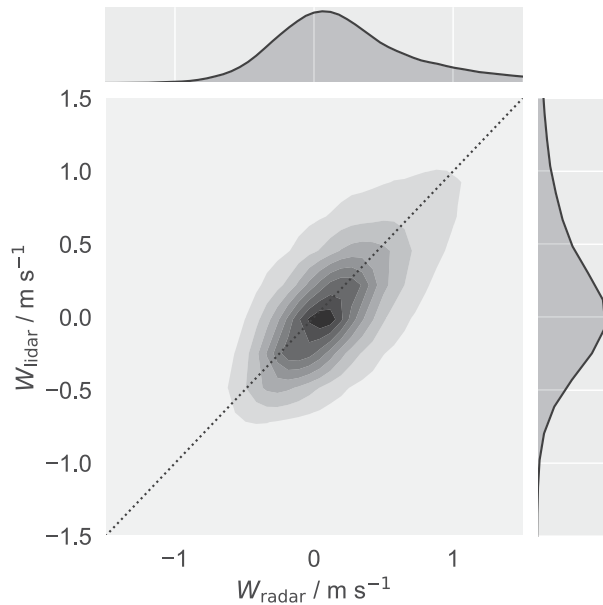


FIG. 4. Intercomparison of Ka-band cloud radar and Doppler lidar vertical velocity measurements. The color indicates the frequency. The measurements were taken on 14 Feb 2018 at the Barbados Cloud Observatory and represent regions in the subcloud layer where hygroscopically grown sea salt particles were present.

cloud parameters. Based on the parameters cloud depth and cloud-base height, all clouds not identified as shallow cumulus are removed (see Fig. 5b). The vertical velocity inside and below the remaining clouds is shown in Fig. 5c.

To calculate the mass flux profile, we use the combined vertical velocity measurements in Fig. 5c and derive first the

fraction of up- and downward motion. The results are shown in Fig. 6a and show below cloud base a higher fraction of downward than upward motion. Similar up- and downdraft fractions indicate isotropic turbulence, but in this case it could also suggest that the region below the shallow cumulus clouds might be governed by a narrow updraft region, which could be surrounded by weaker downdrafts.

Note that, because we expect the radar to disproportionately measure updraft air, as this better supports the development and suspension of larger particles, the lidar detects both, ascending and descending areas. This leads to a higher fraction of up- and downward motions in Fig. 6a than a cloud fraction derived by only a radar instrument.

Figure 6b shows that the updrafts in the subcloud layer are stronger than the downdrafts, which indicates the expected skewness of turbulent motion in a layer driven from warming below (Moeng and Rotunno 1990).

The mass flux profiles in Fig. 6c are calculated with Eq. (4) and cover, based on the combination of the data from Doppler radar and Doppler lidar, the region inside the cloud and below cloud base. Here, the mass flux profile,  $M = M_u + M_d$ , shows below cloud base a maximum in the subcloud layer ( $\sim 300$  m) and is close to zero near cloud base and near ground, the latter for obvious reasons. Above the cloud base, the mass flux profile is increasing, because as soon an air parcel reaches the lifting condensation level, which is represented by the cloud-base height, condensation sets in and the additional vaporization enthalpy allows the expansional work to be accomplished with less change in temperature, which increases the parcel buoyancy, often enough to sustain the further development of the cloud. The maximum of the in-cloud averaged shallow convective mass flux is therefore at an altitude where the product of vertical velocity and cloud fraction shows the highest values

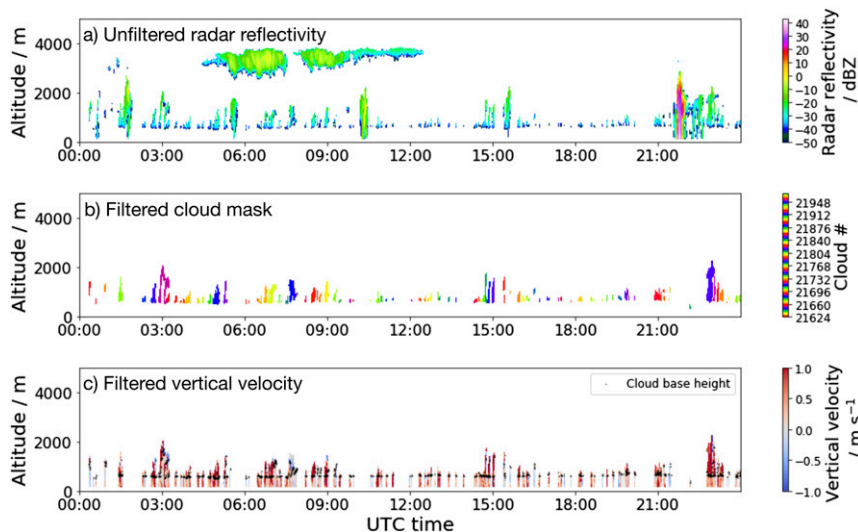


FIG. 5. (a) Radar reflectivity of the Ka-band radar from 28 Mar 2018. (b) Applied cloud mask to radar data. (c) Vertical velocity measurements from the Doppler lidar below and from the Doppler radar inside the clouds. The black dots represent cloud-base height, as detected by the radar. A filter is applied in (b) and (c) to only focus on shallow cumulus clouds.

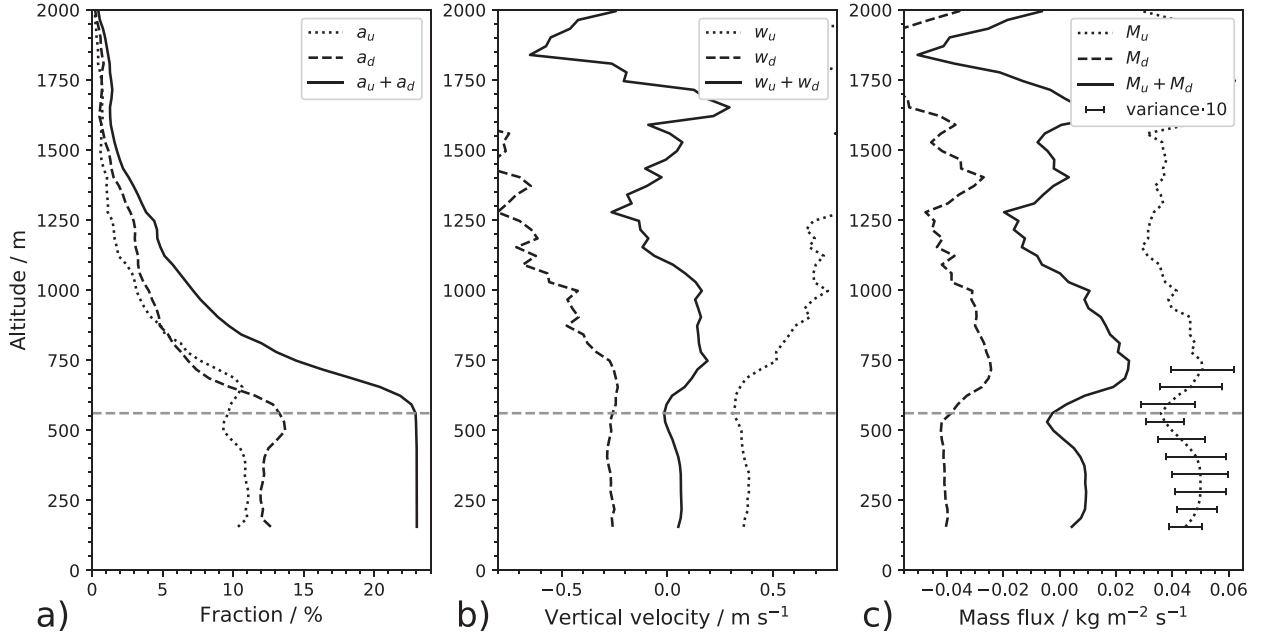


FIG. 6. Vertical profiles of the combined Doppler radar and Doppler lidar dataset from 28 Mar 2018. The horizontal dashed line represents the averaged cloud-base height. (a) The fraction of up- and downdrafts and their sum is shown. (b) The vertical velocity of up- and downward motions and their average is shown. (c) The calculated mass flux profiles based on Eq. (4). The error bars indicate the variance (magnified by factor of 10) of the upward-directed mass flux in the subcloud layer and around the cloud base.

(around 700 m). In the following we refer to this kind of profile as canonical mass flux profile, as it is what is expected for shallow cumulus (Siebesma et al. 2003), with one local maximum in the subcloud layer and another local maximum inside the cloud. This combination of Doppler radar and Doppler lidar data shows for the first time that the estimation of mass flux profiles through the entire boundary layer are possible.

#### b. Correlation between cloud-base mass flux and subcloud-layer velocity scale

In this section, we will use mass flux measurements at the BCO (as estimated by the methods presented in section 5a) and compare them with a hypothesis by Grant (2001), who analyzed large-eddy simulations and found that the cloud-base mass flux is just proportional to the subcloud-layer convective velocity scale. The hypothesis is based on the assumption that the turbulent kinetic energy (TKE) flux  $\overline{w'E_{z_i}}$  is associated with the kinetic energy that forms the roots of the cumulus clouds (LeMone and Pennell 1976):

$$\overline{w'E_{z_i}} = m_b w_*^2. \quad (5)$$

The specific mass flux  $m_b$  describes the mass flux at cloud-base height and represents the ratio of the real mass flux and the air density  $\rho$ . Therefore, its unit is  $\text{m s}^{-1}$ . The subcloud-layer convective velocity scale is represented by

$$w_* = \left( \frac{g}{\theta_v} \overline{w'E_{z_i}} z_i \right)^{1/3} \quad (6)$$

with the acceleration due to gravity  $g$ , the virtual potential temperature  $\theta_v$ , and the mixed layer depth  $z_i$ . Following the calculations by Grant (2001) Eq. (5) leads to

$$m_b = \left[ \frac{1}{2}(1 - \alpha) - A_\varepsilon \right] w_* \quad (7)$$

with the constants  $\alpha = 0.2$  and  $A_\varepsilon = 0.37$  (Stull 1988), which are consistent with measurements (Guillemet et al. 1983). Based on Eq. (7) the cloud base mass flux is just proportional to the subcloud-layer convective velocity scale:

$$m_b = 0.03 w_*. \quad (8)$$

In the following, we will use the remote sensing measurements at the BCO to evaluate this relationship. For this reason, we have to estimate the shallow convective mass flux at cloud base,  $m_b$ , and the convective velocity scale of the subcloud layer,  $w_*$ . To sample the large-scale conditions, which can be covered with measurements longer than 20 h (see section 4), we estimate both parameters for entire shallow cumulus days in 2018. We define a shallow cumulus day as a day with a canonical mass flux profile, like the one in Fig. 6c, which has two local maxima, one in the subcloud layer and one inside the cloud.

Estimating  $w_*$  is challenging, because at the BCO is no instrument located to measure  $\overline{w'E_{z_i}}$  [see Eq. (6)] directly. For this reason, we estimate  $w_*$  from the well-known profiles  $w'^2/w_*^2$  (Lenschow et al. 1980; Fig. 4c), which we assume to be constant with a maximum value in the subcloud layer of 0.4 (van Heerwaarden and Mellado 2016). Based on this assumption we calculate  $w_*$  with:

$$w_* = \sqrt{\frac{w'^2}{0.4}}. \quad (9)$$

Therefore, we only have to estimate the turbulent part

$$w' = \sqrt{(w - \bar{w})^2} \quad (10)$$

of the vertical velocity in the subcloud layer. In contrast to Fig. 5c we take Doppler lidar measurements from the whole subcloud layer (below and in-between shallow cumulus clouds) and keep the high sampling rate of  $1.3 \text{ s}^{-1}$ . As an example, the vertical profiles of  $\bar{w}$ ,  $w'$ , and  $w_*$  for the 28 March 2018 are given in Fig. 7.

To finally compare the BCO measurements with the simulations from Grant (2001) we plot the maximum value of  $w_*$  in the subcloud layer (see Fig. 7) against the upward directed mass flux (see dotted line in Fig. 6c) at cloud-base height. This method was applied for 61 days in 2018 and each dot in Fig. 8a represents one day with a canonical mass flux profile. The averages for the 61 mass flux profiles and the belonging vertical velocities are given in Figs. 8b and 8c, respectively. The result for the 28 March 2018 is represented by the star in Fig. 8a. Considering all measurements shows little evidence of a meaningful correlation between  $m_b$  and  $w_*$ . The majority of the analyzed days in Fig. 8a are in a small convective velocity scale range between  $0.4$  and  $0.8 \text{ m s}^{-1}$  and close to the tropical simulations from Grant (2001), which are around  $0.7 \text{ m s}^{-1}$ . This is plausible, because these four simulations from Grant (2001) are based on the Barbados Oceanographic and Meteorological Experiment [BOMEX; Holland (1970)] and the Atlantic Trade-wind Experiment [ATEX; Augstein et al. (1974)], which took place in the same region. The other simulation from Grant (2001) with a velocity scale around  $1.3 \text{ m s}^{-1}$  is based on data obtained in the midlatitudes over land instead. To cover the whole velocity scale, it would be useful to perform similar measurements in other regions, outside of the tropics. Nevertheless, even if the BCO measurements have a similar velocity scale like the LES, their mass flux at cloud base shows a much stronger variation with the majority of the measurements between  $0.01$  and  $0.04 \text{ m s}^{-1}$ .

That the variation for the mass flux measurements is larger than for the LES might be caused by the different large-scale conditions, for instance large-scale convergence or divergence in the subcloud layer as hypothesized by Malkus (1958) and as has recently been demonstrated by George et al. (2021). While the measurements at the BCO are always influenced by changing large-scale conditions, the LES studies use, according to Grant and Brown (1999), prescribed or constant settings. In conclusion, the comparison of our measurements with the simulations from Grant (2001) might indicate that the large-scale conditions influence the shallow convective mass flux more than would be inferred from using LES under homogeneous conditions.

## 6. Summary

Measuring the shallow convective mass flux is important, because parameterizations of shallow cumulus clouds in GCM simulations are based on a mass flux approach. To identify if

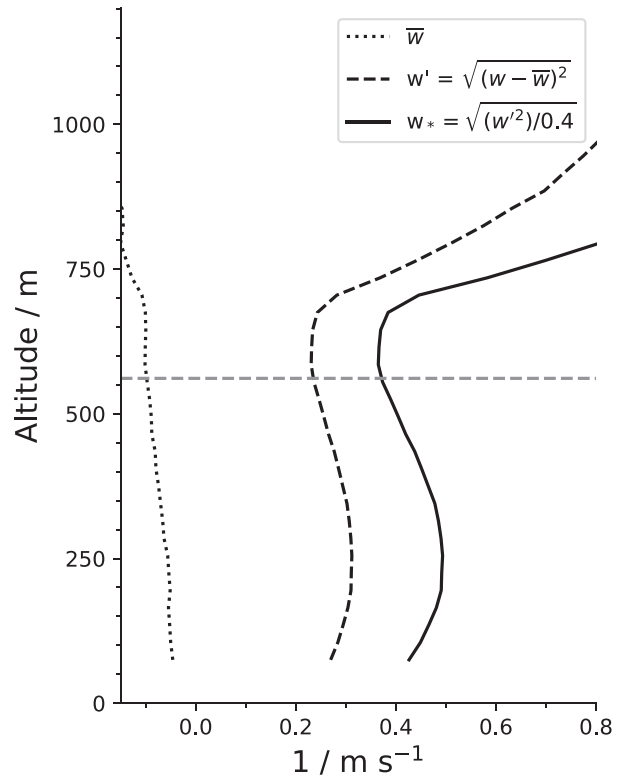


FIG. 7. Vertical profiles of  $\bar{w}$ ,  $w'$ , and  $w_*$  for 28 Mar 2018. The horizontal dashed line represents the cloud-base height.

these parameterizations are correct, comparisons with observations are necessary. In this paper we raised the question, how much the mass flux varies and how this can be used to test factors that may be responsible for its variation. Grant (2001) showed with LES that  $m_b \sim w_*$ . However, Lamer et al. (2015) indicated that the mass flux is mainly influenced by the cloud fraction,  $a$ . To analyze which factor is the dominant one, we used active remote sensing measurements of shallow cumulus clouds taken at the BCO over a time period of 30 months and analyzed vertical profiles of cloud fraction, vertical velocity and the derived mass flux.

With this extended dataset we can confirm that the shallow convective mass flux has a strong relationship with the cloud fraction and the vertical velocity just plays a secondary role, which gave us the opportunity to determine a linear equation which can be used as a rough estimate to calculate the mass flux of shallow cumulus clouds by just knowing the cloud fraction.

We also found that a canonical shallow convective mass flux profile at the BCO has a peak value of  $0.03 \text{ kg m}^{-2} \text{ s}^{-1}$  at an altitude of  $\sim 730 \text{ m}$ , which is close to cloud base. This peak value agrees with a prior study from Ghate et al. (2011), who performed measurements at the Azores Islands. The good agreement indicates that the mass flux profiles of shallow cumulus clouds might be similar at different measurement regions. This is not entirely unexpected as surface buoyancy fluxes are mostly controlled by radiative cooling, which is similar over the oceans in situations where subsidence prevails.

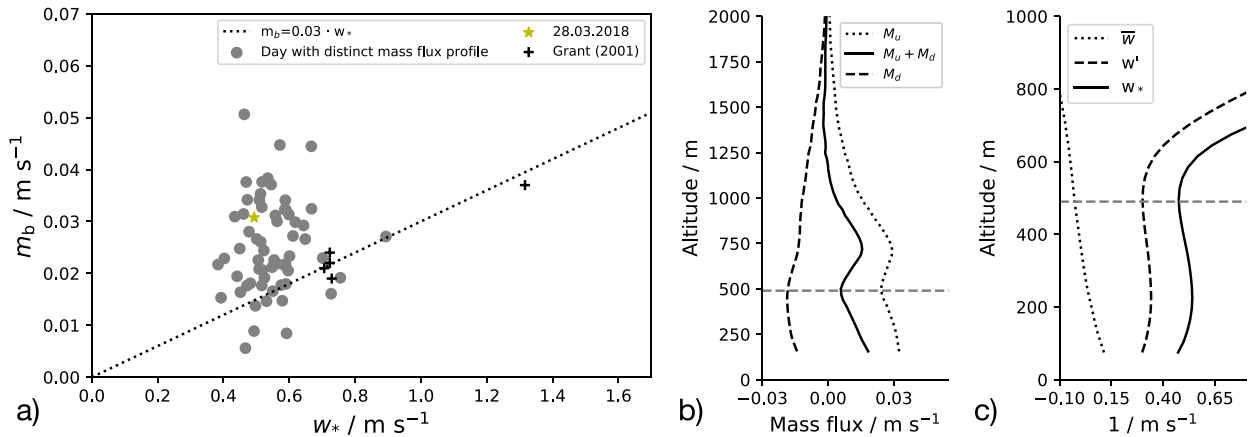


FIG. 8. (a) Convective velocity scale in dependence of shallow cumulus cloud-base mass flux. Each dot represents a day in 2018 with a canonical mass flux profile. From these days, the maximum value of  $w_*$  in the subcloud layer is plotted against the upward-directed mass flux  $m_b$  at cloud-base height. The dotted line and the crosses represent the linear relationship and the different simulations, respectively, given in Grant (2001). (b) Average of the 61 canonical mass flux profiles, separated in upward ( $M_u$ ), downward ( $M_d$ ), and up- and downward motions. (c) Vertical profiles of  $\bar{w}$ ,  $w'$ , and  $w_*$  averaged over the 61 canonical mass flux profiles.

To identify the uncertainty caused by fix point measurements, a simple simulation of a cloud field with a given cloud fraction was performed to identify how long the sampling interval at the BCO needs to be, to avoid uncertainties caused by sampling errors from point measurements. The results indicate that cloud measurements at the BCO are representative when they are longer than two hours. The large-scale conditions, which are influenced by the weather, can be covered with measurements longer than 20 h. For this reason, we sampled in this study over 24 h.

The dependence between  $m_b \sim w_*$  was analyzed by combining for the first time Doppler radar and Doppler lidar data to retrieve vertical velocity and mass flux profiles through the entire boundary layer. Based on this approach we calculated  $m_b$  for 61 days with a canonical mass flux profile and compared it to  $w_*$ .

The results show that for the BCO measurements, the cloud-base mass flux varies significantly for similar convective velocity scales appearing to refute the idea, which was presented in Grant (2001) that  $w_*$  is a major control on the shallow cumulus mass flux. We hypothesize that this is caused by the changing large-scale conditions, which are defined in LES as constant or prescribed. This suggests that the large-scale conditions, like the cloud fraction (we showed similar to Lamer et al. (2015) that it has a strong relationship with the mass flux), might play a more important role for the development of the shallow convective mass flux than is usually assumed in LES studies. To quantify how much the large-scale conditions influence the shallow convective mass flux at the BCO, a future step could be to analyze large-scale measurements from research campaigns like EUREC<sup>4</sup>A (Stevens et al. 2021; Bony et al. 2017) or reanalysis data.

*Acknowledgments.* Scientific support was given by Mirjana Sakradzija, Juan Pedro Mellado, Anna E. Luebke, Ann Kristin Naumann, and Cathy Hohenegger. Special thanks to Lutz

Hirsch, Friedhelm Jansen, Ilya Serikov, David A. Farrell, Marvin Forde, Björn Brüggmann, and Ludwig Worbes to keep the Barbados Cloud Observatory running since 2010. We also would like to thank two anonymous reviewers and Editor C. Rozoff, who had very helpful comments regarding this publication. Access to primary Barbados Cloud Observatory data are provided here: <https://www.mpimet.mpg.de/en/science/the-atmosphere-in-the-earth-system/working-groups/tropical-cloud-observation/barbadosstation1/instrumentation-and-data/>.

## REFERENCES

- Albrecht, B. A., 1981: Parameterization of trade-cumulus cloud amounts. *J. Atmos. Sci.*, **38**, 97–105, [https://doi.org/10.1175/1520-0469\(1981\)038<0097:POTCCA>2.0.CO;2](https://doi.org/10.1175/1520-0469(1981)038<0097:POTCCA>2.0.CO;2).
- Arakawa, A., and W. H. Schubert, 1974: Interaction of a cumulus cloud ensemble with the large-scale environment, Part I. *J. Atmos. Sci.*, **31**, 674–701, [https://doi.org/10.1175/1520-0469\(1974\)031<0674:IOACCE>2.0.CO;2](https://doi.org/10.1175/1520-0469(1974)031<0674:IOACCE>2.0.CO;2).
- Augstein, E., H. Schmidt, and F. Ostapoff, 1974: The vertical structure of the atmospheric planetary boundary layer in undisturbed trade winds over the Atlantic Ocean. *Bound.-Layer Meteor.*, **6**, 129–150, <https://doi.org/10.1007/BF00232480>.
- Bony, S., and Coauthors, 2017: EUREC4A: A field campaign to elucidate the couplings between clouds, convection and circulation. *Surv. Geophys.*, **38**, 1529–1568, <https://doi.org/10.1007/s10712-017-9428-0>.
- Bretherton, C. S., J. R. McCaa, and H. Grenier, 2004: A new parameterization for shallow cumulus convection and its application to marine subtropical cloud-topped boundary layers. Part I: Description and 1D results. *Mon. Wea. Rev.*, **132**, 864–882, [https://doi.org/10.1175/1520-0493\(2004\)132<0864:ANPFC>2.0.CO;2](https://doi.org/10.1175/1520-0493(2004)132<0864:ANPFC>2.0.CO;2).
- George, G., B. Stevens, S. Bony, M. Klingebiel, and R. Vogel, 2021: Observed impact of meso-scale vertical motion on cloudiness. *J. Atmos. Sci.*, **78**, 2413–2427, <https://doi.org/10.1175/JAS-D-20-0335.1>.
- Ghate, V. P., M. A. Miller, and L. DiPretore, 2011: Vertical velocity structure of marine boundary layer trade wind cumulus

- clouds. *J. Geophys. Res.*, **116**, D16206, <https://doi.org/10.1029/2010JD015344>.
- Görsdorf, U., V. Lehmann, M. Bauer-Pfundstein, G. Peters, D. Vavriv, V. Vinogradov, and V. Volkov, 2015: A 35-GHz polarimetric Doppler radar for long-term observations of cloud parameters—Description of system and data processing. *J. Atmos. Oceanic Technol.*, **32**, 675–690, <https://doi.org/10.1175/JTECH-D-14-00066.1>.
- Grant, A. L. M., 2001: Cloud-base fluxes in the cumulus-capped boundary layer. *Quart. J. Roy. Meteor. Soc.*, **127**, 407–421, <https://doi.org/10.1002/qj.49712757209>.
- , and A. R. Brown, 1999: A similarity hypothesis for shallow-cumulus transports. *Quart. J. Roy. Meteor. Soc.*, **125**, 1913–1936, <https://doi.org/10.1002/qj.49712555802>.
- Guillemet, B., H. Isaka, and P. Mascart, 1983: Molecular dissipation of turbulent fluctuations in the convective mixed layer Part I: Height variations of dissipation rates. *Bound.-Layer Meteor.*, **27**, 141–162, <https://doi.org/10.1007/BF00239611>.
- Holland, J. Z., 1970: Preliminary report on the BOMEX sea-air interaction program. *Bull. Amer. Meteor. Soc.*, **51**, 809–821, [https://doi.org/10.1175/1520-0477\(1970\)051<0809:PROTBS>2.0.CO;2](https://doi.org/10.1175/1520-0477(1970)051<0809:PROTBS>2.0.CO;2).
- Klingebiel, M., and Coauthors, 2019: Remote sensing of sea salt aerosol below trade wind clouds. *J. Atmos. Sci.*, **76**, 1189–1202, <https://doi.org/10.1175/JAS-D-18-0139.1>.
- Konow, H., 2020: BCO Cloudmask Code v1.0. Zenodo, <https://doi.org/10.5281/zenodo.4312818>.
- Kumar, V. V., C. Jakob, A. Protat, C. R. Williams, and P. T. May, 2015: Mass-flux characteristics of tropical cumulus clouds from wind profiler observations at Darwin, Australia. *J. Atmos. Sci.*, **72**, 1837–1855, <https://doi.org/10.1175/JAS-D-14-0259.1>.
- Lamer, K., P. Kollias, and L. Nuijens, 2015: Observations of the variability of shallow trade wind cumulus cloudiness and mass flux. *J. Geophys. Res. Atmos.*, **120**, 6161–6178, <https://doi.org/10.1002/2014JD022950>.
- Lareau, N. P., Y. Zhang, and S. A. Klein, 2018: Observed boundary layer controls on shallow cumulus at the ARM Southern Great Plains site. *J. Atmos. Sci.*, **75**, 2235–2255, <https://doi.org/10.1175/JAS-D-17-0244.1>.
- LeMone, M. A., and W. T. Pennell, 1976: The relationship of trade wind cumulus distribution to subcloud layer fluxes and structure. *Mon. Wea. Rev.*, **104**, 524–539, [https://doi.org/10.1175/1520-0493\(1976\)104<0524:TROTWC>2.0.CO;2](https://doi.org/10.1175/1520-0493(1976)104<0524:TROTWC>2.0.CO;2).
- Lenschow, D. H., J. C. Wyngaard, and W. T. Pennell, 1980: Mean-field and second-moment budgets in a baroclinic, convective boundary layer. *J. Atmos. Sci.*, **37**, 1313–1326, [https://doi.org/10.1175/1520-0469\(1980\)037<1313:MFASMB>2.0.CO;2](https://doi.org/10.1175/1520-0469(1980)037<1313:MFASMB>2.0.CO;2).
- Lonitz, K., B. Stevens, L. Nuijens, V. Sant, L. Hirsch, and A. Seifert, 2015: The signature of aerosols and meteorology in long-term cloud radar observations of trade wind cumuli. *J. Atmos. Sci.*, **72**, 4643–4659, <https://doi.org/10.1175/JAS-D-14-0348.1>.
- Malkus, J. S., 1958: On the structure of the trade wind moist layer. *Pap. Phys. Oceanogr. Meteor.*, **13** (2), <https://doi.org/10.1575/1912/1065>.
- Moeng, C.-H., and R. Rotunno, 1990: Vertical-velocity skewness in the buoyancy-driven boundary layer. *J. Atmos. Sci.*, **47**, 1149–1162, [https://doi.org/10.1175/1520-0469\(1990\)047<1149:VVSITB>2.0.CO;2](https://doi.org/10.1175/1520-0469(1990)047<1149:VVSITB>2.0.CO;2).
- Neggers, R. A. J., M. Köhler, and A. C. M. Beljaars, 2009: A dual mass flux framework for boundary layer convection. Part I: Transport. *J. Atmos. Sci.*, **66**, 1465–1487, <https://doi.org/10.1175/2008JAS2635.1>.
- Nuijens, L., B. Stevens, and A. P. Siebesma, 2009: The environment of precipitating shallow cumulus convection. *J. Atmos. Sci.*, **66**, 1962–1979, <https://doi.org/10.1175/2008JAS2841.1>.
- , I. Serikov, L. Hirsch, K. Lonitz, and B. Stevens, 2014: The distribution and variability of low-level cloud in the North Atlantic trades. *Quart. J. Roy. Meteor. Soc.*, **140**, 2364–2374, <https://doi.org/10.1002/qj.2307>.
- Pruppacher, H., and J. Klett, 2010: *Microphysics of Clouds and Precipitation*. Atmospheric and Oceanographic Sciences Library, Vol. 18, Springer, 954 pp.
- Riehl, H., 1954: *Tropical Meteorology*. McGraw-Hill, 392 pp.
- Schulz, H., R. M. Eastman, and B. Stevens, 2021: Characterization and evolution of organized shallow convection in the downstream North Atlantic trades. *J. Geophys. Res. Atmos.*, **126**, e2021JD034575, <https://doi.org/10.1029/2021JD034575>.
- Siebert, H., and Coauthors, 2013: The fine-scale structure of the trade wind cumuli over Barbados; an introduction to the CARRIBA project. *Atmos. Chem. Phys.*, **13**, 10061–10077, <https://doi.org/10.5194/acp-13-10061-2013>.
- Siebesma, A. P., and Coauthors, 2003: A large-eddy simulation intercomparison study of shallow cumulus convection. *J. Atmos. Sci.*, **60**, 1201–1219, [https://doi.org/10.1175/1520-0469\(2003\)60<1201:ALESIS>2.0.CO;2](https://doi.org/10.1175/1520-0469(2003)60<1201:ALESIS>2.0.CO;2).
- Stevens, B., 2005: Atmospheric moist convection. *Annu. Rev. Earth Planet. Sci.*, **33**, 605–643, <https://doi.org/10.1146/annurev.earth.33.092203.122658>.
- , and Coauthors, 2016: The Barbados Cloud Observatory: Anchoring investigations of clouds and circulation on the edge of the ITCZ. *Bull. Amer. Meteor. Soc.*, **97**, 787–801, <https://doi.org/10.1175/BAMS-D-14-00247.1>.
- , and Coauthors, 2020: Sugar, gravel, fish and flowers: Mesoscale cloud patterns in the trade winds. *Quart. J. Roy. Meteor. Soc.*, **146**, 141–152, <https://doi.org/10.1002/qj.3662>.
- , and Coauthors, 2021: EUREC4A. *Earth Syst. Sci. Data Discuss.*, <https://doi.org/10.5194/essd-2021-18>, in press.
- Stull, R., 1988: *An Introduction to Boundary Layer Meteorology*. Kluwer Academic, 666 pp.
- Tiedtke, M., 1989: A comprehensive mass flux scheme for cumulus parameterization in large-scale models. *Mon. Wea. Rev.*, **117**, 1779–1800, [https://doi.org/10.1175/1520-0493\(1989\)117<1779:ACMFSF>2.0.CO;2](https://doi.org/10.1175/1520-0493(1989)117<1779:ACMFSF>2.0.CO;2).
- van Heerwaarden, C. C., and J. P. Mellado, 2016: Growth and decay of a convective boundary layer over a surface with a constant temperature. *J. Atmos. Sci.*, **73**, 2165–2177, <https://doi.org/10.1175/JAS-D-15-0315.1>.
- Vial, J., and Coauthors, 2019: A new look at the daily cycle of trade wind cumuli. *J. Adv. Model. Earth Syst.*, **11**, 3148–3166, <https://doi.org/10.1029/2019MS001746>.

Copyright of Journal of the Atmospheric Sciences is the property of American Meteorological Society and its content may not be copied or emailed to multiple sites or posted to a listserv without the copyright holder's express written permission. However, users may print, download, or email articles for individual use.